

5 June 2007

1 Radiation belt electron precipitation into the atmosphere: recovery from a
2 geomagnetic storm

3 Craig J. Rodger

4 Department of Physics, University of Otago, Dunedin, New Zealand

5 Mark A. Clilverd

6 Physical Sciences Division, British Antarctic Survey, Cambridge, United Kingdom

7 Neil R. Thomson and Rory J. Gamble

8 Department of Physics, University of Otago, Dunedin, New Zealand

9 Annika Seppälä

10 Finnish Meteorological Institute, Helsinki, Finland.

11 Esa Turunen

12 Sodankylä Geophysical Observatory, Sodankylä, Finland.

13 Nigel P. Meredith

14 Physical Sciences Division, British Antarctic Survey, Cambridge, United Kingdom

15 Michel Parrot

16 Laboratoire de Physique et Chimie de l'Environnement, Orleans, France

17 Jean-André Sauvaud

18 Centre d'Etude Spatiale des Rayonnements, Toulouse, France

19 Jean-Jacques Berthelier

20 Centre d'Etudes des Environnements Terrestre et Planétaires, Saint Maur des Fosses, France

1 **Abstract.** Large geomagnetic storms are associated with electron population changes in the
2 outer radiation belt and the slot region, often leading to significant increases in the relativistic
3 electron population. The increased population decays in part through the loss, i.e., precipitation
4 from the bounce loss cone, of highly energized electrons into the middle and upper atmosphere
5 (30-90 km). However, direct satellite observations of energetic electrons in the bounce loss
6 cone are very rare due to its small angular width. In this study we have analyzed ground-based
7 subionospheric radio wave observations of electrons from the bounce loss cone at $L=3.2$ during
8 and after a geomagnetic disturbance which occurred in September 2005. Relativistic electron
9 precipitation into the atmosphere leads to large changes in observed subionospheric amplitudes.
10 Satellite-observed energy spectra from the CRRES and DEMETER spacecraft were used as an
11 input to an ionospheric chemistry and subionospheric propagation model, describing the
12 ionospheric ionization modifications caused by precipitating electrons. We find that the peak
13 precipitated fluxes of >150 keV electrons into the atmosphere were 3500 ± 300 el. $\text{cm}^{-2}\text{s}^{-1}$ at
14 midday and 185 ± 15 el. $\text{cm}^{-2}\text{s}^{-1}$ at midnight.

15 For six days following the storm onset the midday precipitated fluxes are approximately 20
16 times larger than observed at midnight, consistent with observed day/night patterns of
17 plasmaspheric hiss intensities. The variation in DEMETER observed wave power at $L=3.2$ in
18 the plasmaspheric hiss frequency band shows similar time variation to that seen in the
19 precipitating particles. Consequently, plasmaspheric hiss with frequencies below ~ 500 Hz
20 appears to be the principal loss mechanism for energetic electrons in the inner zone of the outer
21 radiation belts during the non-storm time periods of this study, although off-equatorial chorus
22 waves could contribute when the plasmopause is $L < 3.0$.

23 1. Introduction

1 The behavior of high energy electrons trapped in the Earth's Van Allen radiation belts has
2 been extensively studied, through both experimental and theoretical techniques. During quiet
3 times, energetic radiation belt electrons are distributed into two belts divided by the "electron
4 slot" at $L \sim 2.5$. In the more than four decades since the discovery of the belts [*Van Allen, 1997*],
5 it has proved difficult to confirm the principal source and loss mechanisms that control
6 radiation belt particles [*Walt, 1996*]. It has been recognized for some time that the loss of
7 radiation belt electrons in the inner magnetosphere is probably dominated by both pitch angle
8 scattering in wave-particle interactions with whistler mode waves and Coulomb scattering.
9 Collisions with neutral atmospheric constituents are the dominant loss process for energetic
10 electrons (>100 keV) only in the inner-most parts of the radiation belts ($L < 1.3$) [*Walt, 1996*], as
11 demonstrated by the comparison of calculated decay rates with the observed loss of electrons
12 injected by the 1962 Starfish nuclear weapon test (Figure 7.3 of *Walt [1994]*). For higher L -
13 shells, radiation belt particle lifetimes are many orders of magnitude shorter than those
14 predicted from atmospheric collisions, such that other loss processes are clearly dominant.
15 Above $L \sim 1.5$ Coulomb collision-driven losses are generally less important than those driven by
16 whistler mode waves, including plasmaspheric hiss, lightning-generated whistlers, and
17 manmade transmissions [*Abel and Thorne, 1998*]. The electron slot is believed to result from
18 enhanced electron loss rates occurring in this region. Much attention has been given to the role
19 of plasmaspheric hiss in maintaining the electron slot [*Lyons and Williams, 1984*], although it
20 has been suggested that lightning generated whistlers may also be significant in this region
21 [e.g., *Lauben et al., 2001*]. Other calculations suggest that all 3 types of whistler mode waves
22 may play important roles in the loss of energetic electrons in the inner magnetosphere [*Abel*
23 *and Thorne, 1998*].

24 Relatively small changes in the outflow of particles from the Sun can trigger geomagnetic
25 storms [*Sharma et al., 2004*], which produce large changes in radiation belt populations.

1 Typically, the relativistic electron population drops out during the main phase of a storm,
2 recovering on a time scale of ~ 1 day to a level that may or may not be greater than the pre-
3 storm level (but can be several orders of magnitude larger). Essentially all geomagnetic storms
4 substantially alter the electron radiation belt populations [Reeves *et al.*, 2003], in which
5 precipitation losses play a major role [Green *et al.*, 2004]. A significant fraction of the particles
6 are lost into the atmosphere [Horne, 2002; Friedel *et al.*, 2002; Clilverd *et al.*, 2006a], although
7 storm-time non-adiabatic magnetic field changes also led to losses through magnetopause
8 shadowing [e.g. Ukhorskiy *et al.*, 2006].

9 Large geomagnetic storms are associated with radiation belt electron population changes in
10 the outer radiation belt, the electron slot region, and in rare cases the inner radiation belt ($L < 2$)
11 [Baker *et al.*, 2004], where lifetimes are extremely large and hence the increases are long-lived.
12 An example of this was provided by SAMPEX satellite observations of relativistic electrons
13 during a series of large storms that took place in October-November 2003 which show that the
14 normal peak of electron fluxes around $L \approx 4.0$ was displaced far inward to $L < 2.5$ for a period of
15 at least two weeks. The period between 29 October and 4 November 2003, widely known as the
16 Halloween storms, lead to a 10^4 increase in relativistic electron population in the slot region
17 [Baker *et al.*, 2004]. This period was also associated with a number of "anomalies" in
18 spacecraft in Earth orbit and beyond, and in some cases, failures [Webb and Allen, 2004]. It has
19 been suggested that the very large and rapid increases in trapped electron populations provide
20 strong evidence for acceleration processes driven by very low frequency (VLF) whistler mode
21 chorus [Horne *et al.*, 2005].

22 The new population of 2-6 MeV electrons observed during two injections into the slot region
23 at $L \approx 2.5$ decayed in an exponential manner, with e-folding lifetimes of 4.6 and 2.9 days.
24 However, due to the very large increases in the 2-6 MeV electron fluxes at $L \approx 2.5$ and the two
25 injections which occurred in this period, the fluxes in the slot did not return to normal until 3-4

1 weeks after the second injection [*Baker et al.*, 2004]. It is generally understood that the
2 exponential loss was due to cyclotron resonant interactions with VLF waves near the equatorial
3 zone [*Tsurutani and Lakhina*, 1997]. Pitch angle scattering of energetic radiation belt electrons
4 [*Kennel and Petschek*, 1966] by whistler mode waves drives some resonant electrons into the
5 bounce loss cone, resulting in their precipitation into the atmosphere. Direct satellite
6 observations of energetic electrons in the bounce loss cone are very rare. For most of the outer
7 radiation belts, the loss cone is too narrow to be clearly resolved by existing satellite-borne
8 particle detectors.

9 The effect of "pumping up" the radiation belts is eventually translated to the Earth by the
10 loss, i.e., precipitation, of highly energized electrons into the middle and upper atmosphere (30-
11 90 km). The precipitation of energetic electrons changes the atmospheric radiation balance
12 through the production of ozone destroying species which, in turn, modify climate forcing
13 [*Haigh et al.*, 2005]. Energetic electron precipitation results in enhancement of odd nitrogen
14 (NO_x) and odd hydrogen (HO_x), which play a key role in the ozone balance of the middle
15 atmosphere because they destroy odd oxygen through catalytic reactions [*Brasseur and*
16 *Solomon*, 1986]. When this precipitation occurs during the winter darkness, the long-lived NO_x
17 produced is confined by the polar vortex, and within it descends downward to stratospheric
18 altitudes throughout the winter [*Callis et al.*, 1996, *Seppälä et al.*, 2007]; according to recent
19 model results the following ozone reductions in the stratosphere lead to changes in temperature
20 and could possibly effect atmospheric circulation as well as the variation in the zonal winds
21 (QBO, Quasi Biennial Oscillation) [*Elias and de Artigas*, 2003; *Rozanov et al.*, 2005;
22 *Langematz et al.*, 2005].

23 For electrons >100 keV, the bulk of the precipitated energy is deposited into the middle and
24 upper atmospheric levels (~ 30 -90 km), and hence causes the lower ionospheric boundary (the
25 D-region), to shift downwards. One of the few experimental techniques which can probe these

1 altitudes uses VLF electromagnetic radiation, trapped between the lower ionosphere and the
2 Earth [*Barr et al.*, 2000]. The nature of the received radio waves is largely determined by
3 propagation between these boundaries [e.g., *Cummer et al.*, 2000]. Significant variations in the
4 received amplitude and/or phase of fixed frequency VLF transmissions arise from changes in
5 the lower ionosphere, for example, the additional ionization produced by energetic particle
6 precipitation. VLF radio wave propagation has been shown to be sensitive to relativistic
7 electron precipitation events during geomagnetic disturbances [*Thorne and Larsen*, 1976;
8 *Clilverd et al.*, 2006a]. The effect on the signals can be either an increase or decrease in signal
9 amplitude, depending on the modal mixture of each signal observed. Further discussion on the
10 use of subionospheric VLF propagation as a remote sensing probe can be found in recent
11 review articles [e.g., *Barr et al.*, 2000; *Rodger*, 2003]. Observations of subionospheric VLF
12 transmissions permit observers to study energetic particle precipitation from locations remote
13 from the actual precipitation region.

14 In this study we analyze ground-based measurements of ionospheric ionization changes
15 observed during and after a geomagnetic disturbance which occurred in September 2005. This
16 geomagnetic disturbance led to increases in the electron fluxes in the slot and inner edge of the
17 outer radiation belt. Our subionospheric radio wave observations show that while energetic
18 protons from a solar proton event strike the high-latitude polar atmosphere, there is also
19 relativistic electron precipitation occurring at $L \approx 3$. This highly energetic electron precipitation
20 leads to large changes in subionospheric amplitudes, for both day- and night-time conditions.
21 Measurements of electron fluxes are provided by instruments onboard the Combined Release
22 and Radiation Effects Satellite (CRRES) and DEMETER satellites, describing the changes in
23 flux and energy spectrum. The observed energy spectra are used as an input to an ionospheric
24 chemistry and subionospheric propagation model, to describe the nature of the ionosphere
25 modified by precipitating electrons from the radiation belts. The combination of satellite and

1 subionospheric measurements allows us to determine the time-varying electron precipitation
2 fluxes into the atmosphere following a storm time injection into the inner edge of the outer
3 radiation belt.

4 **2. Geophysical Conditions**

5 **2.1 Summary of activity**

6 In August-September 2005 there were a series of 3 major geomagnetic disturbances as
7 recorded by the D_{st} index, each one of which was associated with a >10 times increase in the
8 solar wind density and coronal mass ejections from the Sun. We focus on the last of the 3
9 disturbances due to subionospheric data we have available, as outlined in the section below. On
10 7 September 2005 the GOES spacecraft recorded an X17 solar flare which produced a solar
11 proton event at the Earth shortly afterwards. Proton fluxes at GOES orbits were increased for
12 about a week. The X17 flare was followed over the next week by a series of flares, some of
13 which were also greater than X1. During this time a GOES-detected X6.2 flare was associated
14 with a SOHO reported "Halo" Coronal Mass Ejection (CME) on 9 September 2005, with
15 subsequent "Halo" CMEs on the 10th and 11th of September. This disturbed time period
16 triggered a geomagnetic storm on 11 September 2005, with D_{st} reaching -120 nT and K_p
17 reaching 8. A summary of the geophysical conditions from 1 September 2005 is shown in
18 Figure 1. The top panel shows the GOES-measured proton fluxes, the middle panel the D_{st}
19 index, and the lower panel the K_p index. This plot shows the time delay between the solar
20 proton event seen in the upper panel, associated with a Halo CME launched from the Sun and a
21 solar flare, and the geomagnetic storm seen in the lower two panels triggered by the arrival of
22 the CME at the Earth.

23 **2.2 Satellite observations of the radiation belts**

1 The geomagnetic storm of 11 September 2005 led to an increase in the energetic electron
2 population in the inner edge of the outer radiation belt. Figure 2 shows the evolution with time
3 in satellite measured >150 keV integral electron flux at $L=3.2$ in the drift loss cone, observed
4 by the IDP instrument onboard the DEMETER satellite. We do not include flux measurements
5 made inside the South Atlantic Magnetic Anomaly. DEMETER is the first of the Myriade
6 series of microsattelites developed by the Centre National d'Etudes Spatiales for low-cost
7 science missions, and was placed in a circular Sun-synchronous polar orbit at an altitude of
8 710 km at the end of June 2004. The IDP spectrometer [*Sauvaud et al.*, 2006] is unusual in that
9 it has very high energy resolution; in normal "survey" mode the instrument measures electron
10 fluxes in the drift loss cone with energies from 70 keV to 2.34 MeV using 128 energy channels.
11 DEMETER observations at $L=3.2$ indicate that the typical >150 keV integral electron flux in
12 the drift loss cone is $\sim 2 \times 10^2$ el. $\text{cm}^{-2}\text{s}^{-1}\text{sr}^{-1}$ which occurs outside the time range shown in this
13 figure. Geomagnetic storms in late August 2005 boost the >150 keV fluxes to $\sim 2 \times 10^5$ el. $\text{cm}^{-2}\text{s}^{-1}\text{sr}^{-1}$,
14 after which it decays as seen in Figure 2 in early September. After the 11 September 2005
15 geomagnetic storm DEMETER shows that the electron fluxes in the drift loss cone increases by
16 a factor of ~ 1000 above ambient conditions, and a factor of 100 above the pre-storm flux
17 levels. The fluxes decay to within a factor of 5 of the ambient levels/noise floor over 14 days,
18 after which there is a large data-gap in the DEMETER data (several weeks).

19 The DEMETER observations are consistent with the typical behavior of energetic electron
20 increases at $L=3.05$ reported by CRRES. There were 5 events during the CRRES mission that
21 resulted in perpendicular fluxes of 1.09 MeV electrons greater than $1000 \text{ cm}^{-2}\text{s}^{-1}\text{sr}^{-1}\text{keV}^{-1}$ at
22 $L=3.05$. After each event the fluxes decayed gradually on a timescale of ~ 5.5 days either to
23 quiet time levels or until another flux increase, all increases being caused by enhanced
24 magnetic activity [*Meredith et al.*, 2006a]. Unlike DEMETER, which measures electrons in the
25 drift loss cone and is in low Earth orbit, CRRES was placed on a highly elliptical

1 geosynchronous transfer orbit with a perigee of 305 km and an apogee of 35,768 km, sweeping
2 through the heart of the radiation belts approximately 5 times per day on average, and thus
3 measuring trapped fluxes near the geomagnetic equator. For this reason we cannot make a "like
4 with like" comparison between the measurements of the two spacecraft. The relatively long
5 lifetime of CRRES, providing multiple energy-channel observations of energetic radiation belt
6 electrons, allows an indication of "typical" storm-time increases and their subsequent decay to
7 normal levels. However, CRRES was launched on 25 July 1990 and operated for 15 months
8 and thus cannot provide direct observations for the disturbance in mid-September 2005.

9 Figure 3 shows an example of the typical perpendicular electron flux spectra reported by the
10 Medium Electrons A (MEA) experiment onboard CRRES following enhanced magnetic
11 activity. The MEA instrument, which used momentum analysis in a solenoidal field, had 17
12 energy channels ranging from 153 keV to 1.582 MeV [*Vampola et al.*, 1992]. This particular
13 example is from 20 June 1991, following a geomagnetic storm which occurred on 17 June. The
14 figure shows the trapped electron flux spectra for the 17 MEA energy channels. Also shown is
15 a power-law fit to this flux spectrum (gray line), used to extend the energy range when
16 considering the atmospheric precipitation as outlined below. The power law fit is in the form of
17 $10^{-\gamma E}$ where $\gamma=1.2 \times 10^{-3} \text{ keV}^{-1}$. The thin line in Figure 3 shows the comparison with the
18 DEMETER-observed spectrum for electrons in the drift-loss cone at $L=3.2$ on 12 September
19 2005, where the flux values have been shifted upwards by a factor of 60 to overlay with the
20 CRRES fluxes. The crosses indicate the energy channels, and emphasize the difference
21 between the two instrument's energy resolution. There is a very good agreement between the
22 typical CRRES post-storm trapped flux spectrum and the energy spectrum reported by
23 DEMETER in the drift-loss cone across all energies. CRRES measured trapped fluxes about
24 the geomagnetic equator, while DEMETER fluxes describe the drift-loss cone. While neither
25 instrument provides direct measurements of the particles precipitating in a specific part of the

1 world, the agreement between the two provides strong evidence that this spectrum will provide
2 a reasonable description of that in the bounce loss cone precipitating into the atmosphere and
3 measured by our ground-based instruments. Based on Figure 3 we therefore make use of the
4 fitted energy spectrum and the associated trapped CRRES magnitudes to determine the
5 magnitude of the energetic precipitation into the atmosphere during the mid-September 2005
6 period.

7 **3. Subionospheric Experimental Observations**

8 **3.1 Experimental setup**

9 Here we use narrow band subionospheric VLF data from a 24.0 kHz transmitter (call sign
10 NAA, 44.6°N, 67.3°W, $L=3$) located in Cutler, Maine and received at three European sites.
11 While NAA is often taken to radiate 1 MW, in mid-late 2005 the transmitter was radiating
12 about 600 kW. The receivers are located at: Cambridge, England (52.3°N, 0°E, $L=2.3$), Ny
13 Ålesund, Svalbard (79°N, 11°E, $L=18.3$), and Sodankylä, Finland (67°N, 23°E, $L=5.1$). These
14 sites are part of the Antarctic-Arctic Radiation-belt Dynamic Deposition VLF Atmospheric
15 Research Konsortia (AARDDVARK). More information on AARDDVARK can be found at
16 the Konsortia website: http://www.physics.otago.ac.nz/space/AARDDVARK_homepage.htm.
17 Figure 4 shows the location of the transmitter site (circle), the receiver sites (diamonds), and
18 the modeling location (54°N, 35°W, asterisk), and also indicates the great circle propagation
19 paths between the transmitter and receivers. The receivers at these locations were AbsPAL
20 (Cambridge) [Thomson *et al.*, 2005], and OmniPAL (Ny Ålesund, Sodankylä) [Dowden *et al.*,
21 1998] instruments, both of which log the amplitude and phase of the MSK modulated
22 transmissions from NAA. The midpoints of the transmitter-receiver great circle paths are at
23 $L\approx 3.2$ for NAA-Cambridge, $L\approx 12$ for NAA- Ny Ålesund, and $L\approx 7.5$ for NAA- Sodankylä.

24 **3.2 Modeling subionospheric propagation**

1 Mesospheric ionization effects on VLF/LF wave propagation can be modeled using the Long
 2 Wave Propagation Code [LWPC, *Ferguson and Snyder*, 1990]. LWPC models VLF signal
 3 propagation from any point on Earth to any other point. Given electron density profile
 4 parameters for the upper boundary conditions, LWPC calculates the expected amplitude and
 5 phase of the VLF signal at the reception point. For undisturbed time periods, the D-region
 6 electron density altitude-profile is often expressed through a Wait ionosphere, defined in terms
 7 of a sharpness parameter β and a reference height h' [*Wait and Spies*, 1964], and the electron
 8 number density (i.e., electrons per m^{-3}), N_e , increases exponentially with altitude z ,

$$9 \quad N_e(z) = 1.43 \times 10^{13} \exp(-0.15 h') \times \exp((\beta-0.15)(z- h')). \quad (1)$$

10 For example, the amplitude of NAA at Cambridge at midday for undisturbed ionospheric
 11 conditions has been experimentally measured at 60-61 dB above $1 \mu\text{Vm}^{-1}$. Using the daytime
 12 ionospheric model of *McRae and Thomson* [2000], where $\beta=0.37 \text{ km}^{-1}$ and $h'=72.5 \text{ km}$, LWPC
 13 models the received amplitude of NAA at Cambridge as 60.7 dB above $1 \mu\text{Vm}^{-1}$, showing the
 14 power of the model. The LWPC model can be used to investigate changes in the lower
 15 ionosphere as long as the induced changes to the electron density altitude-profiles are known.
 16 One approach is to provide this using the Sodankylä Ion Chemistry model [SIC, version 6.8,
 17 *Verronen et al.*, 2005] to determine the effects of the additional ionization caused by particle
 18 precipitation. The combination of LWPC and the SIC model to understand VLF observations
 19 has been reported in previous studies [e.g., *Clilverd et al.*, 2005; 2006b]. The modeling of
 20 electron density changes produced by particle precipitation is described in Section 4.0, which
 21 also includes a full description of SIC.

22 3.3 Subionospheric observations

23 Figure 5 shows the NAA received amplitude (diamonds) at Ny Ålesund (NYA; top panels),
 24 Sodankylä (SGO; middle panels), and Cambridge (CAM; lower panels) for midday (right
 25 panels) and midnight (left panels) conditions. Note that the experimental data is in dB relative

1 to an arbitrary reference level. In all 6 panels, the dash-dot lines show the expected amplitudes
2 for undisturbed conditions. The heavy black horizontal line indicates the main period where
3 $K_p > 6$ (10-13 September). The onset of the solar proton event shown in Figure 1 is indicated by
4 the vertical dashed line. The solid line in the top two sets of panels is the predicted NAA
5 amplitude modeling using a combination of LWPC and the SIC model to simulate the effect of
6 the solar protons following the approach outlined in *Clilverd et al.* [2006b]. As expected the
7 proton simulations show that the two top (high L -shell) receivers are strongly influenced by
8 precipitation of protons during the solar proton event. The modeling indicates that we would
9 not expect the proton effects to last beyond the 15th September during the night, and the 20th
10 September during the day, which is in very good agreement with the observations at Ny
11 Ålesund (NYA). However, the observed amplitude changes at Sodankylä (SGO) are larger and
12 longer lived than predicted from the proton forcing modeling. In addition, there are substantial
13 changes in the observed NAA amplitude at Cambridge, which will only be marginally impacted
14 by protons due to rigidity cutoffs [*Störmer*, 1930], even taking into account the levels of
15 geomagnetic activity [*Rodger et al.*, 2006]. This provides strong evidence for the precipitation
16 of energetic electrons from the radiation belts occurring at lower L -shells, with the path from
17 NAA to CAM dominated by the electron precipitation.

18 We therefore concentrate on the NAA observations from Cambridge, for which the great
19 circle path largely passes along the $L=3.2$ contour, and so is only likely to be affected by the
20 CRRES and DEMETER reported radiation belt flux enhancements described above. Additional
21 evidence for this comes from the NAA to CAM observed amplitudes in early September, which
22 indicate precipitation from the late August/early September geomagnetic storms. This is in
23 contrast with NAA to NYA, the received amplitudes of which agree well with the expected
24 undisturbed conditions. As shown in the lower panels of Figure 5, the ionospheric forcing from
25 the energetic electron precipitation leads to a 2.4 ± 0.3 dB increase in the amplitude of NAA

1 observed at Cambridge at midday, but a 14 ± 1 dB decrease in the same quantity observed at
2 midnight. By modeling the time-varying amplitude changes of NAA observed at Cambridge we
3 can determine the precipitation rate of electrons from the radiation belts along this great circle
4 path.

5 **4. Ionospheric effects of precipitation**

6 The ionization rate due to precipitating energetic electrons is calculated by an application of
7 the expressions in *Rees* [1989], expanded to higher energies based on *Goldberg and Jackman*
8 [1984]. The background neutral atmosphere is calculated using the NRLMSISE-00 neutral
9 atmospheric model [*Picone et al.*, 2002]. The energy spectrum is taken from the fit to the
10 CRRES observations shown in Figure 3, extrapolated over the energy range 150-3000 keV. As
11 the precipitating flux magnitude is unknown, and the topic of our study, we consider what
12 electron precipitation flux best reproduces our subionospheric radio wave data using the fitted
13 energy spectrum.

14 **4.1 Sodankylä Ion Chemistry model**

15 In order to determine the impact of the energetic precipitation on the lower ionosphere, the
16 ionization rate must be combined with a chemistry model to determine the change in electron
17 number density. Figure 6 shows the impact of the CRRES-described precipitating electrons on
18 the lower ionosphere at midday (upper panel) and midnight (lower panel), calculated by the
19 Sodankylä Ion Chemistry model (solid lines). The Sodankylä Ion Chemistry (SIC, version 6.8)
20 model is a 1-D ion and neutral chemistry model designed for ionospheric D-region studies,
21 solving the concentrations of 63 ions, including 27 negative ions, and 13 neutral species at
22 altitudes across 20–150 km. The model has recently been discussed by *Verronen et al.* [2005],
23 building on original work by *Turunen et al.* [1996] and *Verronen et al.* [2002]. A detailed

1 overview of the model was given in *Verronen et al.* [2005], but we summarize in a similar way
2 here to provide background for this study.

3 In the SIC model several hundred reactions are implemented, plus additional external forcing
4 due to solar radiation (1–422.5 nm), electron and proton precipitation, and galactic cosmic
5 radiation. Initial descriptions of the model are provided by *Turunen et al.* [1996], with neutral
6 species modifications described by *Verronen et al.* [2002]. Solar flux is calculated with the
7 SOLAR2000 model (version 2.21) [*Tobiska et al.*, 2000]. The scattered component of solar
8 Lyman- α flux is included using the empirical approximation given by *Thomas and Bowman*
9 [1986]. The SIC model includes vertical transport [*Chabrilat et al.*, 2002] which takes into
10 account molecular diffusion coefficients [*Banks and Kockarts*, 1973]. The background neutral
11 atmosphere is calculated using the MSISE-90 model [*Hedin*, 1991] and tables given by
12 *Shimazaki* [1984].

13 Figure 6 shows the "ambient" electron number density profiles for midday and midnight
14 (lines with crosses), calculated by the SIC model with no particle precipitation on 13
15 September 2005 at the location (54°N, 35°W) marked on Figure 4, i.e., the half-way point on
16 the NAA-CAM path. The SIC-calculated precipitation-modified electron number density
17 profiles presented in this figure (solid line) represent the stable equilibrium state for the
18 electron number density including the effect of a constant CRRES-described electron
19 precipitation source, with a stable state reached in <10 minutes after the precipitation starts.
20 The upper panel shows the resulting enhanced electron densities at midday created by energetic
21 precipitation with a >150 keV integral flux magnitude (measured in $\text{el. cm}^{-2}\text{s}^{-1}$) that is 4×10^{-5} of
22 the trapped flux reported by CRRES (Figure 4), while the lower panel shows this for midnight
23 and a flux magnitude that is 2×10^{-6} of the trapped flux reported by CRRES. The choice of the
24 daytime and nighttime precipitation flux magnitudes will become apparent in Section 5.

1 The energetic electron precipitation significantly alters the electron number density in Figure
 2 6 over the altitude range of ~55-90 km, by 1.5-2 orders of magnitude at ~70 km. Note that this
 3 reflects the significance of the precipitation, and not the limits of the 150-3000 keV energy
 4 range. Precipitating 3 MeV electrons produce ionization rates which are largest at ~47 km
 5 altitude, which due to the spectral roll-off in population have a minor effect as seen in Figure 6.
 6 In contrast, 150 keV electrons affect altitudes above about ~80 km. Taking the lower limit of
 7 150 keV does not significantly alter the electron profiles; for example, taking the lower limit as
 8 10 keV would lead to no change in Figure 6 for daytime conditions, and a very slight increase
 9 in electron density for nighttime altitudes above 85 km (not shown), too small to make a
 10 significant change in the VLF propagation conditions relative to the much more significant
 11 electron density increases at lower altitudes.

12 **4.2 "Simple" ionospheric electron model**

13 The full SIC model is somewhat too complex for exploring the most-likely precipitation flux
 14 magnitudes with LWPC, as the computation time is relatively high. For this reason, we made use
 15 of a considerably simpler model to describe the balance of electron number density in the lower
 16 ionosphere, based on that given by *Rodger et al.* [1998]. In this model the evolution of the
 17 electron density in time is governed by the equation

$$18 \quad \frac{\partial N_e}{\partial t} = q - \beta N_e - \alpha N_e^2 \quad (2)$$

19 where q is the ionization rate, α is the recombination coefficient (m^3s^{-1}), and β is the attachment
 20 rate (s^{-1}). *Rodger et al.* [1998] provides expressions for the altitude variation of α and β ,
 21 appropriate for nighttime conditions. A comparison of the SIC calculations with the electron
 22 number densities calculated using the Rodger expressions, for the same ionization rates,
 23 showed that the Rodger expressions provided acceptable agreement with the SIC nighttime
 24 calculations, but that the Rodger approach gave very different answers when compared with the

1 SIC daytime calculations. However, through trial and error modified recombination and
 2 attachment coefficients have been determined which do an excellent job at reproducing both
 3 the daytime and nighttime SIC electron number densities, but with much lower computational
 4 loads. Note that these expressions can only provide information on electron number densities,
 5 unlike SIC which solves the ion and neutral concentrations. A comparison between SIC and the
 6 simple model is shown in Figure 6, where the simple model is shown as a dotted line with
 7 circles.

8 **Nighttime:** Small changes are made in the *Rodger et al.* [1998] expressions to provide the best
 9 quality agreement with SIC nighttime calculations. For altitudes above 80 km,

$$10 \quad \alpha_{eff} = 2.5 \times 10^{-11} \sqrt{300/T_e} \text{ m}^3\text{s}^{-1} \quad (3)$$

11 where T_e is the electron temperature, while for altitudes of 80 km and below,

$$12 \quad \alpha_{eff} = 2.0 \times 10^{-12} \left(T_e/300 \right)^{-0.55} \text{ m}^3\text{s}^{-1} \quad (4)$$

13 The attachment rate in *Rodger et al.* [1998] is described through $\beta = \beta_1 + \beta_2$, where β_1 is
 14 defined in Table 1 of that paper, and β_2 in equation (22). In the modified expressions,

$$15 \quad \beta = (\beta_1 + \beta_2)/1.4 \quad (5)$$

16 **Daytime:** The original Rodger expressions are insufficient to describe the daytime electron
 17 density levels, particularly attachment-reactions which occur much more slowly due to solar
 18 input. For altitudes above 84 km,

$$19 \quad \alpha_{eff} = 3 \times 10^{-12} \sqrt{300/T_e} \text{ m}^3\text{s}^{-1} \quad (6)$$

20 while for altitudes of 84 km and below,

$$21 \quad \alpha_{eff} = 5.0 \times 10^{-13} \left(T_e/300 \right)^{-0.55} \text{ m}^3\text{s}^{-1} \quad (7)$$

22 The attachment rate for daytime is best modeled by

$$\beta = (\beta_1 + \beta_2)/75 \quad (8)$$

5. Modeling the precipitation effect on subionospheric propagation

The electron number density profiles determined using the simple ionospheric electron model for varying precipitation flux magnitudes are used as input to the LWPC subionospheric propagation model, thus modeling the effect of precipitation on the NAA received amplitudes at Cambridge. An undisturbed electron density profile is used which reproduces the received NAA amplitudes at Cambridge, specified by the Wait ionosphere $\beta=0.37 \text{ km}^{-1}$ and $h'=72.5 \text{ km}$ for midday and $\beta=0.5 \text{ km}^{-1}$ and $h'=85 \text{ km}$ for midnight. The difference in the LWPC-modeled received amplitude changes for varying precipitation magnitudes is shown in Figure 7, for midday (top panel) and midnight (bottom panel) ionospheric conditions. The horizontal dotted lines indicate the peak experimentally observed amplitude differences, $+2.4\pm 0.3 \text{ dB}$ at midday on 13 September 2005 and $-14\pm 1 \text{ dB}$ at midnight on 12 September 2005. The peak experimental amplitude difference at midday is best modeled by a flux magnitude that is $\sim 4.5 \times 10^{-5}$ of the typical post-storm trapped flux reported by CRRES, while for midnight the experimental data is best modeled by a flux magnitude ratio of $\sim 2.4 \times 10^{-6}$. This equates to peak precipitated fluxes of $>150 \text{ keV}$ electrons of $3500\pm 300 \text{ el. cm}^{-2}\text{s}^{-1}$ at midday and $185\pm 15 \text{ el. cm}^{-2}\text{s}^{-1}$ at midnight. For both midday and midnight conditions, multiple precipitation flux levels can lead to the same amplitude difference, particularly for the midnight case, where there is a very strong modal discontinuity for flux ratios of about 4×10^{-6} . In general it should be possible to discriminate between the possible fluxes by assuming near-continuity in the day-to-day precipitation levels, although this should be confirmed by follow-on studies.

6. Observed precipitation from subionospheric propagation measurements

1 Figure 8 shows the time variation of the >150 keV electron flux precipitated into the
2 atmosphere, determined from the time-varying amplitude differences of NAA received at
3 Cambridge ($L=3.2$) shown in Figure 5 combined with the modeled response shown in Figure 7.
4 Both daytime (diamonds) and nighttime (asterisks) precipitating fluxes are seen to increase
5 around the start of the large geomagnetic storm on 11/12 September 2005, followed by a
6 recovery towards undisturbed conditions over the following 10-15 days. During the six days
7 following the storm onset the midday precipitated fluxes are approximately 20 times larger than
8 observed at midnight. This day-night precipitation flux difference is consistent with the
9 statistical pattern of plasmaspheric hiss intensities reported around the geomagnetic equator
10 using CRRES observations. During geomagnetically disturbed conditions ($AE^* > 150$ nT) the
11 average plasmaspheric hiss intensity in the 0.2-0.5 kHz band was reported to be ~ 10 times
12 stronger on the dayside than the nightside, while at higher frequencies (4-5 kHz) the waves are
13 orders of magnitudes weaker and stronger on the nightside rather than dayside [*Meredith et al.*,
14 Figure 7, 2006b]. At $L=3.2$, 0.5 kHz waves will undergo cyclotron resonance [*Chang and Inan*,
15 1983] with 160 keV electrons, altering the pitch angles of the electrons and potentially driving
16 them into the bounce loss cone such that they can precipitate into the atmosphere. Lower
17 frequencies resonate with higher energy electrons, representative of the >150 keV precipitating
18 fluxes considered in our study, with 1 MeV electrons resonating with waves of ~ 40 Hz. Thus
19 the observed variation in the low-frequency band plasmaspheric hiss could drive the
20 precipitation of energetic electrons, leading to the order of magnitude day-night difference in
21 precipitation fluxes seen in Figure 8.

22 The ICE instrument on the DEMETER spacecraft provides continuous measurements of the
23 power spectrum of one electric field component in the VLF band (*Berthelier et al.*, 2006).
24 Figure 9 shows the daily variation in the mean power spectrum over the frequency band 40-
25 500 Hz for the geographic longitude range 300-360°E and $L=3.2$, i.e., corresponding to the

1 great circle path between NAA and Cambridge. Again, the daytime observations are
2 represented by diamonds while those at night are shown by asterisks. Comparing Figure 8 and
3 Figure 9 shows quite close agreement between the behavior of the 40-500 Hz waves in the
4 plasmaspheric hiss band and the observed precipitating electrons. Note that both the wave
5 power and precipitating particle fluxes vary by a factor of ~ 200 between the period 9-11
6 September 2005, with the daytime wave powers roughly ten times larger than at nighttime, and
7 with a similar ratio between day and night seen in the precipitating fluxes. In the periods where
8 the wave power is larger by night than by day, for example 5-9 September, there is evidence for
9 similar behavior in the precipitating particles. The primary difference between the two plots
10 occurs before 5 September 2005 and after 20 September 2005. For the situation before 5
11 September 2005 large plasmaspheric hiss wave power is present, but strong increases in
12 precipitating particle fluxes were not seen, despite the availability of particles in the radiation
13 belts (Figure 2). In the later case the large plasmaspheric hiss wave power present in the
14 daytime was not associated with a subionospherically-measured increase in precipitation
15 fluxes, perhaps because of a lack of particle availability. Nonetheless, this comparison provides
16 strong evidence that plasmaspheric hiss with frequencies below ~ 500 Hz is the primary driver
17 for the loss of energetic electrons in the inner zone of the outer radiation belts during the non-
18 storm time periods of this study period. However we acknowledge that the driver that leads to
19 the differing precipitation fluxes we observe on the dayside and nightside is not wholly
20 resolved, and the examination of additional similar events will be necessary to confirm the
21 current study.

22 **7. Discussion**

23 *Meredith et al.* [2003b] have shown that the intensities of lower-band VLF chorus, which has
24 frequencies from a tenth to a half of the electron gyrofrequency, are also enhanced during

1 geomagnetic disturbances. However, dawnside equatorial chorus does not reproduce the day-
2 night differences seen in our precipitation fluxes, as it has peak intensities on the morning and
3 evening side. In addition at $L=3.2$ the electron gyrofrequency is 26.6 kHz such that the lower-
4 band chorus resonant energies span $\sim 1-25$ keV, much smaller than required to explain our
5 observed precipitation range. In contrast, off-equatorial lower-band chorus is ~ 100 times
6 stronger on the dayside than the nightside, considerably larger than the factor of 10 difference
7 seen in our precipitation measurements. However, for off equatorial chorus (observed between
8 15 and 30 degrees off the magnetic equator and which is enhanced on the dayside) the resonant
9 energies are much higher ~ 250 keV to ~ 1 MeV. This suggests that off equatorial chorus could
10 contribute to the loss of energetic electrons as has been previously suggested by various authors
11 [e.g. *Horne and Thorne, 2003*].

12 The position of the plasmopause plays an important role in determining what processes may
13 be operating in a particular region at a given time. During strong magnetic activity
14 plasmaspheric hiss is enhanced inside the plasmasphere, principally on the dayside [*Meredith et*
15 *al., 2004*]. In contrast, enhanced whistler mode chorus waves tend to be observed outside of the
16 plasmopause, with the equatorial and mid-latitude waves being observed principally on the
17 dawn-side and day-side respectively [*Meredith et al., 2003a*]. During strong magnetic activity
18 ($K_p^* > 6$) the plasmopause can move inside of $L = 3.0$ [*Carpenter and Anderson, 1992*], where
19 K_p^* is the maximum value of the K_p index in the previous 24 hours. Thus there are some storm-
20 time intervals, notably $\sim 11-14$ and $15-16$ September 2005, when our transmitter-receiver great
21 circle path at $L \approx 3.0$ is likely to be outside of the plasmopause, at least at certain local times.
22 During these intervals there could be a contribution from the off-equatorial (dayside) chorus
23 [e.g. *Horne and Thorne, 2003*]. Using IMAGE EUV measurements taken at 23:38 UT 12
24 September 2005 available from euv.lpl.arizona.edu/, we have confirmed that the nighttime
25 plasmopause was at about $L=3.5$, following the approach outlined in *Goldstein et al. [2003]*.

1 Thus our transmitter-receiver GCP was inside the plasmapause during the storm time of mid-11
2 to mid-13 September when $K_p \approx 6$. At the non-storm times our transmitter-receiver GCP at $L \approx$
3 3.0 will be inside the plasmasphere, and as such chorus will not play a role during these times.
4 The period of gradual decay occurring after 17 September 2005 seen in Figure 2 is thus most
5 likely due to plasmaspheric hiss, whereas the period of decay between 11 and 17 September
6 could be due to a combination of both hiss and chorus.

7 The time-varying observations of electron losses from the inner zone of the outer radiation
8 belts shown in Figure 8 will provide an important constraint to radiation belt electron
9 acceleration and loss models currently under development [e.g., *Horne et al.*, 2005]. In
10 addition, the fluxes reported in this study can be used to drive atmospheric chemistry models
11 [e.g., *Verronen et al.*, 2005] and test the relative significance of this precipitation to neutral
12 atmospheric chemistry.

13 **8. Summary**

14 The effect of "pumping up" the radiation belts during geomagnetic storms is translated to the
15 Earth by the loss, i.e., precipitation, of highly energized electrons into the middle and upper
16 atmosphere (30-90 km). However, direct satellite observations of energetic electrons in the
17 bounce loss cone are very rare due to the small size of the loss cone. In this study we have
18 analyzed ground-based subionospheric radio wave observations of the bounce loss cone during
19 and after a geomagnetic disturbance which occurred in September 2005. After the 11
20 September 2005 geomagnetic storm the particle instrument onboard the DEMETER spacecraft
21 shows that the >150 keV electron fluxes in the drift loss cone at $L=3.2$ increased by a factor of
22 ~ 1000 above ambient conditions. The fluxes decayed to within a factor of 5 of the ambient
23 levels over the following 14 days. The DEMETER-measured electron energy spectrum for the
24 post-storm increase has a gradient consistent with the typical spectra observed by the CRRES

1 spacecraft for injections into the inner zone of the outer radiation belts, despite DEMETER
2 measuring drift loss cone fluxes and CRRES measuring fluxes trapped near the geomagnetic
3 equator.

4 Our subionospheric radio wave observations of the NAA transmitter received at Cambridge
5 during this period show that there is relativistic electron precipitation into the atmosphere
6 occurring at $L \approx 3$. This highly energetic electron precipitation leads to large changes in
7 subionospheric amplitudes, with peak experimentally observed amplitude differences of
8 $+2.4 \pm 0.3$ dB at midday on 13 September 2005 and -14 ± 1 dB at midnight on 12 September
9 2005. The observed energy spectra were used as an input to an ionospheric chemistry and
10 subionospheric propagation model, to describe the nature of the ionospheric ionization
11 modifications caused by the precipitating electrons. The peak precipitated fluxes of >150 keV
12 electrons into the atmosphere were 3500 ± 300 el. $\text{cm}^{-2}\text{s}^{-1}$ at midday and 185 ± 15 el. $\text{cm}^{-2}\text{s}^{-1}$ at
13 midnight.

14 The combination of satellite and subionospheric measurements allowed us to determine the
15 time-varying electron precipitation fluxes following a storm time injection into the inner edge
16 of the outer radiation belt, providing a direct measurement of the losses from the radiation belts
17 into the atmosphere. During the six days following the storm onset the midday precipitated
18 fluxes are approximately 20 times larger than observed at midnight, consistent with observed
19 day/night patterns of plasmaspheric hiss intensities. The variation in DEMETER observed
20 wave power at $L=3.2$ in the plasmaspheric hiss band shows similar time variation to that seen in
21 the precipitating particles. Plasmaspheric hiss with frequencies below ~ 500 Hz appears to be
22 the primary driver for the loss of energetic electrons in the inner zone of the outer radiation
23 belts during the non-storm time periods of this study, although off-equatorial chorus waves
24 could contribute when the plasmopause is $L < 3.0$.

1 **Acknowledgments.** The peak amplitude changes observed at Cambridge correspond to the
2 birthday of our co-author, Annika Seppälä. May her birthdays always bring us such luck! The
3 authors would like to thank Simon Stewart and Robert McCormick, of the University of Otago,
4 for initial software development.

5

6 **References**

- 7 Abel, B., and Thorne, R. M.: Electron scattering loss in earth's inner magnetosphere-2.
8 Sensitivity to model parameters, *J. Geophys. Res.*, 103, 2397-2407, 1998.
- 9 Baker, D.N., S.G. Kanekal, X. Li, et al., An extreme distortion of the Van Allen belt arising from
10 the 'Hallowe'en' solar storm in 2003, *Nature*, vol. 432(7019), pp. 878-880, 2004.
- 11 Banks, P. M., and Kockarts, G.: *Aeronomy*, vol. B, chap. 15, Academic Press, 1973.
- 12 Barr, R., D. L. Jones, and C. J. Rodger, ELF and VLF Radio Waves, *J. Atmos. Sol. Terr. Phys.*,
13 vol. 62(17-18), 1689-1718, 2000.
- 14 Berthelier, J.J., Godefroy, M., Leblanc, F., Malingre, M., Menvielle, M., Lagoutte, D., Brochot,
15 J.Y., Colin, F., Elie, F., Legendre, C., Zamora, P., Benoist, D., Chapuis, Y., Artru, J., ICE,
16 The electric field experiment on DEMETER, *Planet. Space Sci.*, 54 (5), Pages 456-471, 2006.
- 17 Brasseur, G., and Solomon, S.: *Aeronomy of the Middle Atmosphere*, second ed., D. Reidel
18 Publishing Company, Dordrecht, 1986.
- 19 Callis, L. B., D. N. Baker, M. Natarajan, J. B. Blake, R. A. Mewaldt, R. S. Selesnick, J. R.
20 Cummings, A 2-D model simulation of downward transport of NO_y into the stratosphere:
21 Effects on the 1994 austral spring O₃ and NO_y, *Geophys. Res. Lett.*, 23(15), 1905-1908,
22 10.1029/96GL01788, 1996.
- 23 Carpenter, D.L., and R.R. Anderson, An ISEE/whistler model of equatorial electron density in
24 the magnetosphere, *J. Geophys. Res.*, 97, 1097-1108, 1992.

- 1 Chabrillat, S., Kockarts, G., Fonteyn, D., and Brasseur, G.: Impact of molecular diffusion on the
2 CO₂ distribution and the temperature in the mesosphere, *Geophys. Res. Lett.*, 29, 1-4, 2002.
- 3 Chang, H. C., and U. S. Inan, Quasi-relativistic electron precipitation due to interactions with
4 coherent VLF waves in the magnetosphere, *J. Geophys. Res.*, 88, 318-328, 1983.
- 5 Clilverd, M. A., C. J. Rodger, T. Ulich, A. Seppälä, E. Turunen, A. Botman, and N. R. Thomson
6 (2005), Modeling a large solar proton event in the southern polar atmosphere, *J. Geophys.*
7 *Res.*, 110, A09307, doi:10.1029/2004JA010922.
- 8 Clilverd, M. A., C. J. Rodger and Th. Ulich, The importance of atmospheric precipitation in
9 storm-time relativistic electron flux drop outs, *Geophys. Res. Lett.*, 33, L01102,
10 doi:10.1029/2005GL024661, 2006a.
- 11 Clilverd, M. A., A. Seppälä, C. J. Rodger, N. R. Thomson, P. T. Verronen, E. Turunen, T. Ulich,
12 J. Lichtenberger, and P. Steinbach (2006b), Modeling polar ionospheric effects during the
13 October–November 2003 solar proton events, *Radio Sci.*, 41, RS2001,
14 doi:10.1029/2005RS003290.
- 15 Cummer, S. A., Modeling electromagnetic propagation in the earth-ionosphere waveguide, *IEEE*
16 *Transactions on Antennas and Propagation*, vol. 48(9), 1420-1429, 2000.
- 17 Elias A. G., M. Zossi de Artigas, A search for an association between the equatorial stratospheric
18 QBO and solar UV irradiance, *Geophys. Res. Lett.*, 30 (16), 1841,
19 doi:10.1029/2003GL017771, 2003.
- 20 Dowden, R. L., Hardman, S. F., Rodger, C. J., Brundell, J. B.: Logarithmic decay and Doppler
21 shift of plasma associated with sprites, *J. Atmos. Sol. Terr. Phys.*, 60, 741-753, 1998.
- 22 Ferguson, J. A., and F. P. Snyder (1990), Computer programs for assessment of long wavelength
23 radio communications, Tech. Doc. 1773, Natl. Ocean Syst. Cent., San Diego, California.
- 24 Friedel, R.H.W., G.D. Reeves, and T. Obara, Relativistic electron dynamics in the inner
25 magnetosphere - a review, *J. Atmos. Sol. Terr. Phys.*, 64, 265, 2002.

- 1 Goldberg, R. A., and C. H. Jackman, Nighttime auroral energy deposition in the middle
2 atmosphere, *J. Geophys. Res.*, 89(A7), 5581-5596, 1984.
- 3 Goldstein, J., M. Spasojevi, P. H. Reiff, B. R. Sandel, W. T. Forrester, D. L. Gallagher, and B.
4 W. Reinisch (2003), Identifying the plasmopause in IMAGE EUV data using IMAGE RPI in
5 situ steep density gradients, *J. Geophys. Res.*, 108(A4), 1147, doi:10.1029/2002JA009475.
- 6 Green, J. C., T. G. Onsager, T. P. O'Brien, and D. N. Baker (2004), Testing loss mechanisms
7 capable of rapidly depleting relativistic electron flux in the Earth's outer radiation belt, *J.*
8 *Geophys. Res.*, 109, A12211, doi:10.1029/2004JA010579.
- 9 Haigh, J. D., M. Blackburn, and R. Day, The response of tropospheric circulation to
10 perturbations in lower-stratospheric temperature, *J. Climate*, vol. 18(17), pp. 3672-3685,
11 2005.
- 12 Hedin, A. E.: Extension of the MSIS thermospheric model into the middle and lower atmosphere,
13 *J. Geophys. Res.*, 96, 1159-1172, 1991.
- 14 Horne, R.B., The contribution of wave-particle interactions to electron loss and acceleration in
15 the Earth's radiation belts during geomagnetic storms, in *URSI Review of Radio Science 1999-*
16 *2002*, edited by W.R. Stone, pp. 801-828, Wiley, 2002.
- 17 Horne R. B., R. M. Thorne, Relativistic electron acceleration and precipitation during resonant
18 interactions with whistler-mode chorus, *Geophys. Res. Lett.*, 30 (10), 1527,
19 doi:10.1029/2003GL016973, 2003.
- 20 Horne, R.B., R.M. Thorne, Y. Y. Shprits, et al., Wave acceleration of electrons in the Van Allen
21 radiation belts, *Nature*, vol. 437, pp. 227 - 230, 2005.
- 22 Kennel, C. F., and Petschek, H. E.: Limit on stably trapped particle fluxes, *J. Geophys. Res.*,
23 71(1), 1-27, 1966.
- 24 Langematz, U., J. L. Grenfell, K. Matthes, P. Mieth, M. Kunze, B. Steil, and C. Brühl (2005),
25 Chemical effects in 11-year solar cycle simulations with the Freie Universität Berlin Climate

- 1 Middle Atmosphere Model with online chemistry (FUB-CMAM-CHEM), *Geophys. Res.*
2 *Lett.*, 32, L13803, doi:10.1029/2005GL022686.
- 3 Lauben, D. S., U. S. Inan, and T. F. Bell, Precipitation of radiation belt electrons induced by
4 obliquely propagating lightning generated whistlers, *J. Geophys. Res.*, 106, 29745-29770,
5 2001.
- 6 Lyons, L. R., and D. J. Williams, *Quantitative Aspects of Magnetospheric Physics*, Geophysics
7 and Astrophysics Monographs, Kluwer, Hingham, 1984.
- 8 McRae, W. M., and N. R. Thomson, VLF phase and amplitude: daytime ionospheric parameters,
9 *J. Atmos. Sol. Terr. Phys.*, 62, no 7, 609-618, 2000.
- 10 Meredith, N. P., Horne, R. B., Iles, R. H. A., Thorne, R. M., Heynderickx, D., and Anderson, R.
11 R.: Outer zone relativistic electron acceleration associated with substorm-enhanced whistler
12 mode chorus, *J. Geophys. Res.*, 108, art. no. 1016, 2002.
- 13 Meredith N. P., R. M. Thorne, R. B. Horne, D. Summers, B. J. Fraser, R. R. Anderson,
14 Statistical analysis of relativistic electron energies for cyclotron resonance with EMIC
15 waves observed on CRRES, *J. Geophys. Res.*, 108 (A6), 1250,
16 doi:10.1029/2002JA009700, 2003a.
- 17 Meredith N. P., R. B. Horne, R. M. Thorne, R. R. Anderson (2003b), Favored regions for
18 chorus-driven electron acceleration to relativistic energies in the Earth's outer radiation
19 belt, *Geophys. Res. Lett.*, 30 (16), 1871, doi:10.1029/2003GL017698.
- 20 Meredith N. P., R. B. Horne, R. M. Thorne, D. Summers, R. R. Anderson (2004), Substorm
21 dependence of plasmaspheric hiss, *J. Geophys. Res.*, 109, A06209,
22 doi:10.1029/2004JA010387.
- 23 Meredith N. P., R. B. Horne, S. A. Glauert, R. M. Thorne, D. Summers, J. M. Albert, R. R.
24 Anderson, Energetic outer zone electron loss timescales during low geomagnetic activity, *J.*
25 *Geophys. Res.*, 111, A05212, doi:10.1029/2005JA011516, 2006a.

- 1 Meredith N. P., R. B. Horne, M. A. Clilverd, D. Horsfall, R. M. Thorne, R. R. Anderson (2006b),
2 Origins of plasmaspheric hiss, *J. Geophys. Res.*, 111, A09217, doi:10.1029/2006JA011707.
- 3 Picone, J. M., Hedin, A. E., Drob, D. P., and Aikin, A. C.: NRLMSISE-00 empirical model of the
4 atmosphere: Statistical comparisons and scientific issues, *J. Geophys. Res.*, 107(A12), 1468,
5 doi:10.1029/2002JA009430, 2002.
- 6 Rees, M. H.: *Physics and chemistry of the upper atmosphere*, Cambridge University Press,
7 Cambridge, 1989.
- 8 Reeves, G.D., et al., Acceleration and loss of relativistic electrons during geomagnetic storms,
9 *Geophys. Res. Lett.*, vol. 30(10), 1529, doi:10.1029/2002GL016513, 2003.
- 10 Rodger, C. J.: Subionospheric VLF perturbations associated with lightning discharges, *J. Atmos.*
11 *Sol. Terr. Phys.*, 65, 591-606, 2003.
- 12 Rodger, C. J., O. A. Molchanov, and N. R. Thomson, Relaxation of transient ionization in the
13 lower ionosphere, *J. Geophys. Res.*, 103(4), 6969-6975, 1998.
- 14 Rodger, C. J., M. A. Clilverd, P. T. Verronen, Th. Ulich, M. J. Jarvis, and E. Turunen, Dynamic
15 geomagnetic rigidity cutoff variations during a solar proton event, *J. Geophys. Res.*, 111,
16 A04222, doi:10.1029/2005JA011395, 2006.
- 17 Rozanov, E., et al., Atmospheric response to NO_y source due to energetic electron precipitation,
18 *Geophys. Res. Lett.*, 32, L14811, doi:10.1029/2005GL023041, 2005.
- 19 Sauvaud, J.A. T. Moreau, R. Maggiolo, J.-P. Treilhou, C. Jacquy, A. Cros, J. Coutelier, J.
20 Rouzaud, E. Penou and M. Gangloff, (2006), High-energy electron detection onboard
21 DEMETER: The IDP spectrometer, description and first results on the inner belt, *Planet.*
22 *Space. Sci.*, 54 (5), 502-511.
- 23 Seppälä, A., M. A. Clilverd, and C. J. Rodger, NO_x enhancements in the middle atmosphere: The
24 relative significance of Solar Proton Events and the Aurora as a source, *J. Geophys. Res.*, (in
25 review), 2007.

- 1 Sharma, A.S., Y. Kamide, and G.S. Lakhina (eds), *Disturbances in Geospace: The Storm-*
2 *Substorm Relationship*, Geophysical Monograph, 142, Am. Geophys. Union, 2004.
- 3 Shimazaki, T.: *Minor Constituents in the Middle Atmosphere (Developments in Earth and*
4 *Planetary Physics, No 6)*, D. Reidel Publishing Co., Dordrecht, Netherlands, 1984.
- 5 Störmer, C. (1930), *Periodische elektronenbahnen im feld eines elementarmagnetron und ihre*
6 *anwendung auf bruches modellversuche und auf eschenhagens elementarwellen des*
7 *erdmagnetismus*, *Zeitschr. f. Astrophys.*, 1, 237-274.
- 8 Thomas, L., and Bowman, M. R.: *A study of pre-sunrise changes in negative ions and electrons*
9 *in the D-region*, *Annales Geophys.*, 4(3), 219-227, 1986.
- 10 Thomson, N. R., C. J. Rodger, and M. A. Clilverd, *Large solar flares and their ionospheric D-*
11 *region enhancements*, *J. Geophys. Res.*, 110, A06306, doi:10.1029/2005JA011008, 2005.
- 12 Thorne, R. M., and T. R. Larsen (1976), *An investigation of relativistic electron precipitation*
13 *events and their association with magnetic substorm activity*, *J. Geophys. Res.*, 81, 5501-
14 5506.
- 15 Tobiska, W. K., Woods, T., Eparvier, F., Viereck, R., Floyd, L. D. B., Rottman, G., and White,
16 O. R.: *The SOLAR2000 empirical solar irradiance model and forecast tool*, *J. Atmos. Terr.*
17 *Phys.*, 62, 1233-1250, 2000
- 18 Tsurutani, B. T., and Lakhina, G.S.: *Some basic concepts of wave-particle interactions in*
19 *collisionless plasmas*, *Rev. Geophys.*, 35(4), 491-501, 1997.
- 20 Turunen, E., Matveinen, H., Tolvanen, J., and Ranta, H.: *D-region ion chemistry model*, in *STEP*
21 *Handbook of Ionospheric Models*, edited by R. W. Schunk, pp. 1-25, SCOSTEP Secretariat,
22 Boulder, Colorado, USA, 1996.
- 23 Ukhorskiy A. Y., B. J. Anderson, P. C. Brandt, and N. A. Tsyganenko, *Storm time evolution of*
24 *the outer radiation belt: Transport and losses*, *J. Geophys. Res.*, 111, A11S03,
25 doi:10.1029/2006JA011690, 2006.

- 1 Vampola, A. L., Osborn, J. V., and Johnson, B. M.: CRRES Magnetic Electron Spectrometer, J.
2 Spacecr. Rockets, 29, 592, 1992.
- 3 Van Allen, J. A.: Energetic particles in the Earth's external magnetic field, in Discovery of the
4 Magnetosphere, edited by C. S. Gillmor and J. R. Spreiter, History of Geophysics, 7, 235-251,
5 American Geophysical Union, Washington, D.C., 1997.
- 6 Verronen, P. T., Turunen, E., Ulich, Th., and Kyrölä, E.: Modelling the effects of the October
7 1989 solar proton event on mesospheric odd nitrogen using a detailed ion and neutral
8 chemistry model, Ann. Geophys., 20, 1967-1976, 2002.
- 9 Verronen, P. T., Seppälä, A., Clilverd, M. A., Rodger, C. J., Kyrölä, E., Enell, C-F., Ulich, Th.,
10 and Turunen, E.: Diurnal variation of ozone depletion during the October-November 2003
11 solar proton event, J. Geophys. Res., 110(A9), doi:10.1029/2004JA010932, 2005.
- 12 Wait, J. R., and K. P. Spies, Characteristics of the Earth-ionosphere waveguide for VLF radio
13 waves, NBS Tech. Note 300, Nat. Inst. of Stand. and Technol., Gaithersburg, Md., 1964.
- 14 Walt, M., *Introduction to geomagnetically trapped radiation*, Cambridge University Press,
15 Cambridge, 1994.
- 16 Walt, M.: Source and loss processes for radiation belt particles, in Radiation Belts: Models and
17 Standards, edited by J. F. Lemaire et al., Geophysical Monograph, 97, 1-13, American
18 Geophysical Union, Washington, D.C., 1996.
- 19 Webb, D. F. and J. H. Allen, Spacecraft and ground anomalies related to the October-November
20 2003 solar activity. Space Weather 2, doi:10.1029/2004SW000075, 2004.
- 21
- 22 _____
- 23 Jean-Jacques Berthelier, Centre d'Etudes des Environnements Terrestre et Planétaires, 4
24 Avenue de Neptune, Saint Maur des Fosses, France. (email: jean-
25 jacques.berthelier@cetp.ipsl.fr).

1 M. A. Clilverd, and N. P. Meredith, Physical Sciences Division, British Antarctic Survey,
2 High Cross, Madingley Road, Cambridge CB3 0ET, England, U.K. (e-mail:
3 M.Clilverd@bas.ac.uk, nmer@bas.ac.uk).

4 R. J. Gamble, C. J. Rodger, and N. R. Thomson, Department of Physics, University of Otago,
5 P.O. Box 56, Dunedin, New Zealand. (email: rgamble@physics.otago.ac.nz,
6 crodger@physics.otago.ac.nz, thomson@physics.otago.ac.nz).

7 M. Parrot, Laboratoire de Physique et Chimie de l'Environnement, 3A Avenue de la Recherche
8 Scientifique, 45071 Orleans Cedex 2, France (email: mparrot@cnr-orleans.fr).

9 J. A. Sauvaud, Centre d'Etude Spatiale des Rayonnements, 9 Avenue du Colonel Roche 31028,
10 Toulouse Cedex 4, France (email: sauvaud@cesr.fr)

11 A. Seppälä, Earth Observation, Finnish Meteorological Institute, P.O. Box 503 (Vuorikatu 15
12 A), FIN-00101 Helsinki, Finland. (email: Annika.Seppala@fmi.fi).

13 E. Turunen, Sodankylä Geophysical Observatory, Tähteläntie 62, FIN-99600 Sodankylä,
14 Finland. (email: esa@sgo.fi).

15

16

17 RODGER ET AL.: RADIATION BELT ELECTRON PRECIPITATION

18

1 **Figure Captions**

2 **Figure 1.** Summary of geophysical conditions appropriate for this study, starting from 1
3 September 2005. The top panel shows the GOES-measured proton fluxes, the middle panel the
4 D_{st} index, and the lower panel the K_p index.

5 **Figure 2.** Variation with time of the >150 keV electrons at $L=3.2$ observed in the drift loss
6 cone by the DEMETER spacecraft.

7 **Figure 3.** Electron energy spectra at $L\approx 3$, typical of those seen following significant enhanced
8 magnetic activity leading to enhanced trapped electron fluxes. The heavy line shows the
9 trapped flux measurements by CRRES, with the gray line indicating a power law fitting. The
10 thin line shows the contrast with the DEMETER-observed spectra in the drift-loss cone, shifted
11 to overlay with the CRRES fluxes.

12 **Figure 4.** Map showing the location of the transmitter NAA, the VLF receivers (diamonds), and
13 the modeling location. This map also indicates the great circle propagation paths between the
14 transmitter and receivers.

15 **Figure 5.** The received amplitudes of NAA at Ny Ålesund (NYA), Sodankylä (SGO), and
16 Cambridge (CAM) for midday (right panels) and midnight (left panels). In all panels the dash-
17 dot lines shows the expected amplitudes for undisturbed conditions. In the upper four panels the
18 diamonds show the experimental data while the line shows the simulated amplitude changes
19 expected due to solar proton forcing. In the lower two panels the diamonds connected by a line
20 show the experimental data.

21 **Figure 6.** Electron number density profiles with altitude calculated by the SIC-model for
22 undisturbed conditions (line with crosses) and due to forcing by energetic particle precipitation

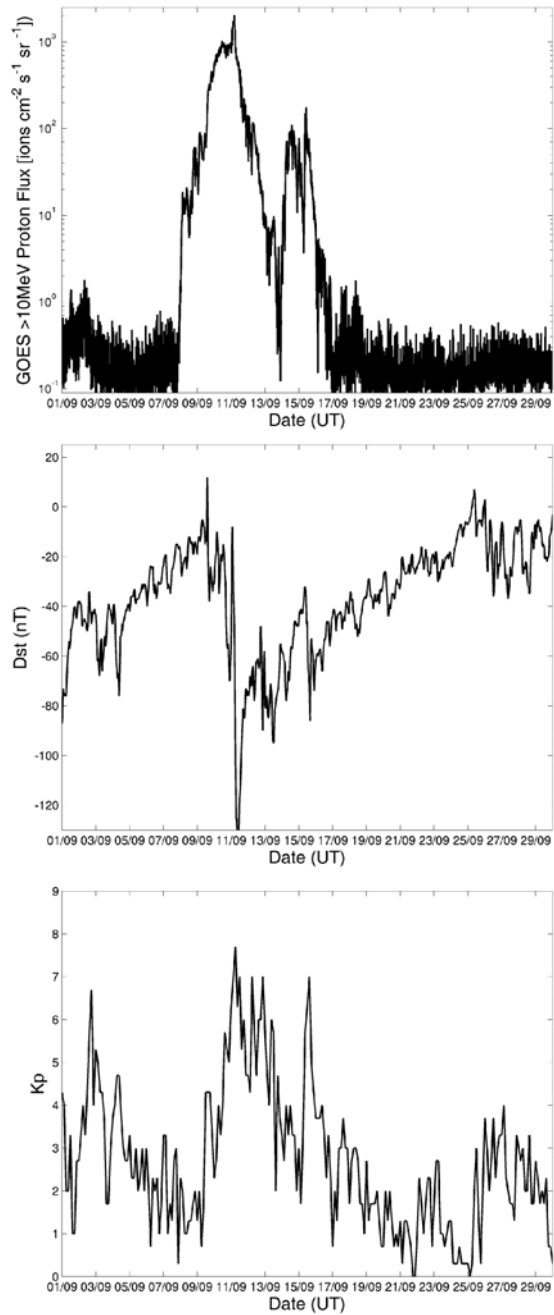
1 (heavy line) for midday and midnight. The dotted line with circles shows the electron density
2 profile calculated using a simple electron density model described in the text.

3 **Figure 7.** LWPC-modeled received amplitude changes for varying precipitation magnitudes.
4 The horizontal dotted lines indicate the peak experimentally observed amplitude differences.

5 **Figure 8.** Time variation of the >150 keV electron flux precipitated into the atmosphere,
6 determined for midday (diamonds) and midnight (asterisks) using the NAA amplitude
7 differences received at Cambridge (Figure 5).

8 **Figure 9.** Time variation of the mean spectral power in the 40-500 Hz frequency band at $L=3.2$
9 and restricted to the geographic longitude range of 300-360°E, observed by the DEMETER
10 spacecraft for day (diamonds) and night (asterisks).

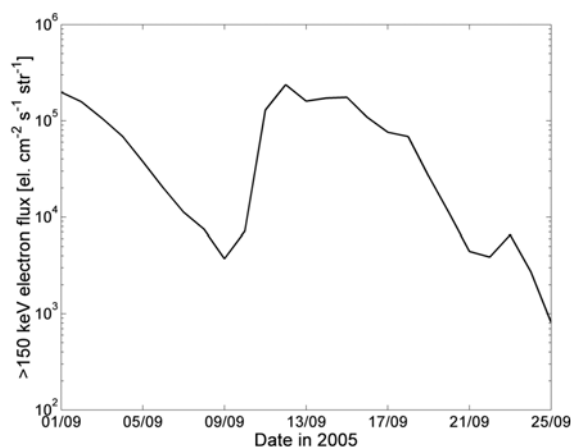
11



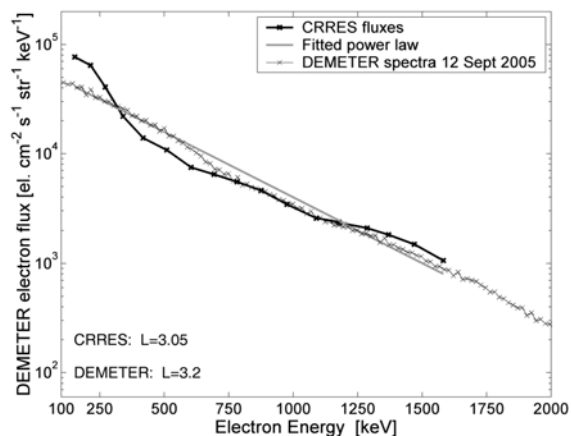
1

2 **Figure 1.** Summary of geophysical conditions appropriate for this study, starting from 1
 3 September 2005. The top panel shows the GOES-measured proton fluxes, the middle panel the
 4 D_{st} index, and the lower panel the K_p index.

5

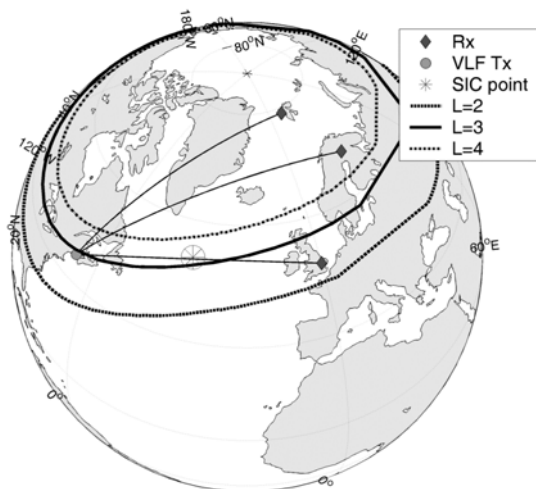


1
2 **Figure 2.** Variation with time of the >150 keV electrons at $L=3.2$ observed in the drift loss
3 cone by the DEMETER spacecraft.



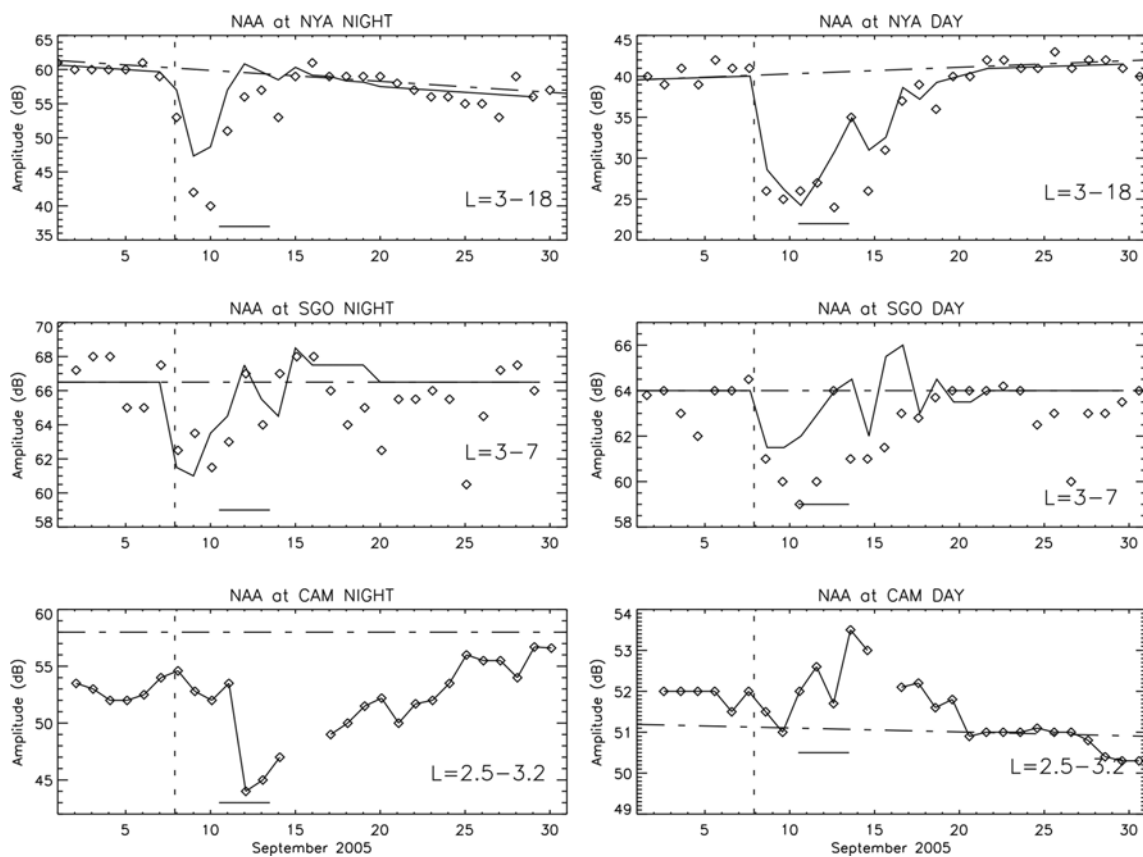
5
6 **Figure 3.** Electron energy spectra at $L \approx 3$, typical of those seen following significant enhanced
7 magnetic activity leading to enhanced trapped electron fluxes. The heavy line shows the
8 trapped flux measurements by CRRES, with the gray line indicating a power law fitting. The
9 thin line shows the contrast with the DEMETER-observed spectra in the drift-loss cone, shifted
10 to overlay with the CRRES fluxes.

11



1
2 **Figure 4.** Map showing the location of the transmitter NAA, the VLF receivers (diamonds), and
3 the modeling location. This map also indicates the great circle propagation paths between the
4 transmitter and receivers.

5

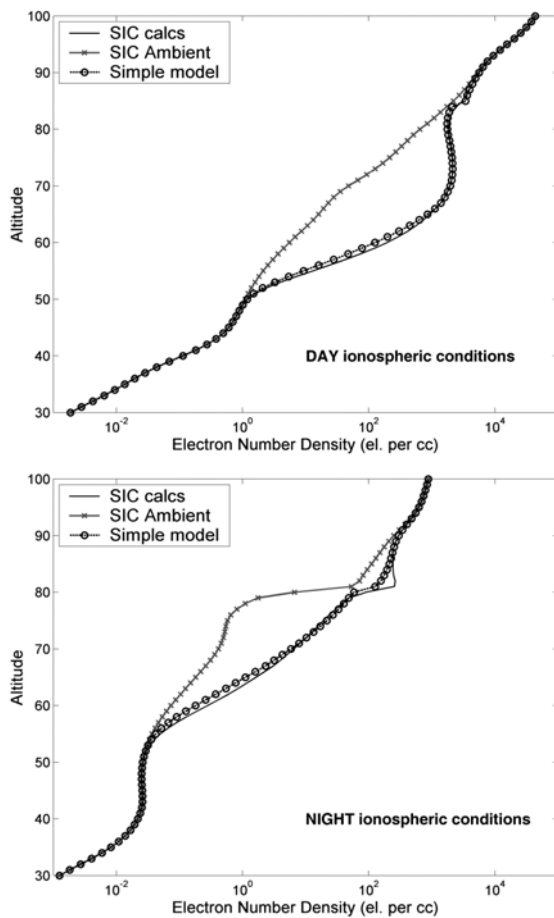


6

1 **Figure 5.** The received amplitudes of NAA at Ny Ålesund (NYA), Sodankylä (SGO), and
 2 Cambridge (CAM) for midday (right panels) and midnight (left panels). In all panels the dash-
 3 dot lines shows the expected amplitudes for undisturbed conditions. In the upper four panels the
 4 diamonds show the experimental data while the line shows the simulated amplitude changes
 5 expected due to solar proton forcing. In the lower two panels the diamonds connected by a line
 6 show the experimental data.

7

8



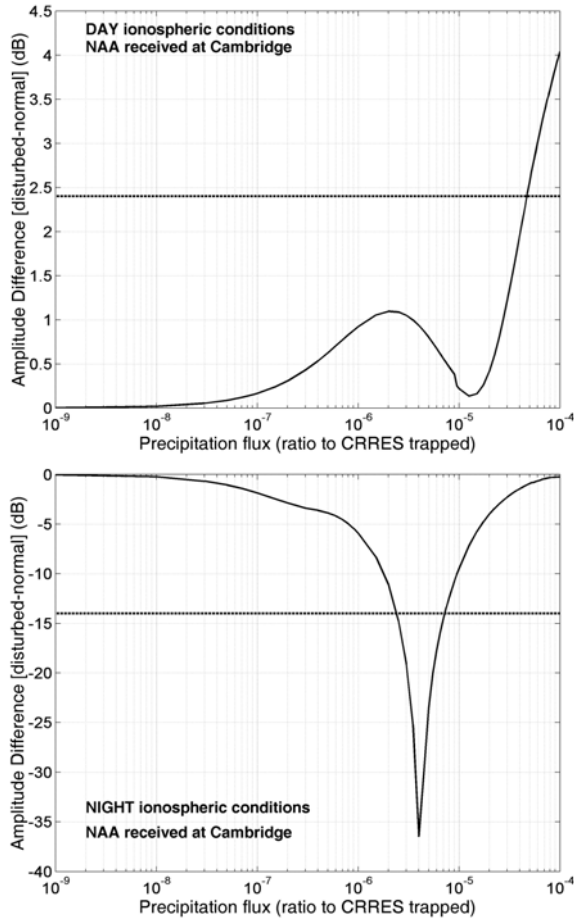
9

10 **Figure 6.** Electron number density profiles with altitude calculated by the SIC-model for
 11 undisturbed conditions (line with crosses) and due to forcing by energetic particle precipitation

1 (heavy line) for midday and midnight. The dotted line with circles shows the electron density
 2 profile calculated using a simple electron density model described in the text.

3

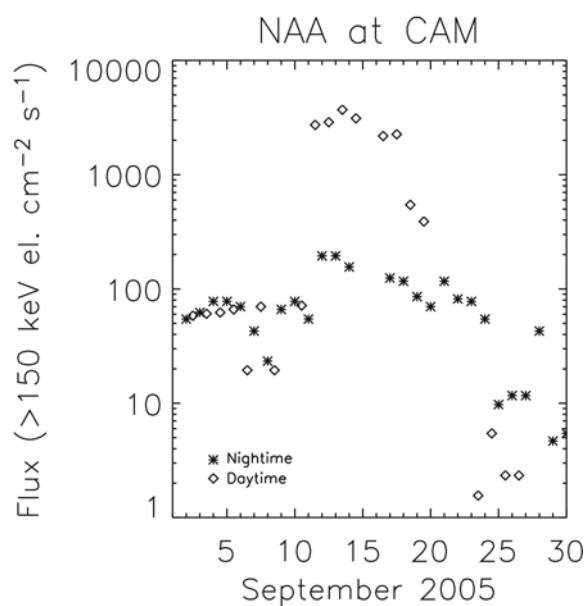
4



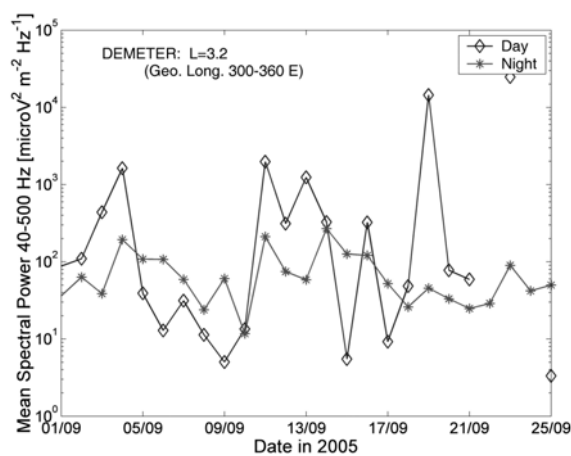
5

6 **Figure 7.** LWPC-modeled received amplitude changes for varying precipitation magnitudes.

7 The horizontal dotted lines indicate the peak experimentally observed amplitude differences.



1
2 **Figure 8.** Time variation of the >150 keV electron flux precipitated into the atmosphere,
3 determined for midday (diamonds) and midnight (asterisks) using the NAA amplitude
4 differences received at Cambridge (Figure 5).



7
8 **Figure 9.** Time variation of the mean spectral power in the 40-500 Hz frequency band at $L=3.2$
9 and restricted to the geographic longitude range of 300-360°E, observed by the DEMETER
10 spacecraft for day (diamonds) and night (asterisks).

11